

Voltage- and temperature-dependent rare-earth dopant contribution to the interfacial magnetic anisotropy

Alejandro O. Leon¹ and Gerrit E. W. Bauer^{2,3,4}

Abstract. The control of magnetic materials and devices by voltages without electric currents holds the promise of power-saving nano-scale devices. Here we study the temperature-dependent voltage control of the magnetic anisotropy caused by rare-earth (RE) local moments at an interface between a magnetic metal and a non-magnetic insulator, such as Co|(RE)|MgO. Based on a Stevens operator representation of crystal and applied field effects, we find large dominantly quadrupolar intrinsic and field-induced interface anisotropies at room temperature. We suggest improved functionalities of transition metal tunnel junctions by dusting their interfaces with rare earths.

¹Departamento de Física, Facultad de Ciencias Naturales, Matemática y del Medio Ambiente, Universidad Tecnológica Metropolitana, Las Palmeras 3360, Ñuñoa 780-0003, Santiago, Chile

² WPI-AIMR, Tohoku University, Sendai 980-8577, Japan

³ Institute for Materials Research & CSRN, Tohoku University, Sendai 980-8577, Japan

⁴ Zernike Institute for Advanced Materials, Groningen University, The Netherlands

E-mail: a Leon@utem.cl

March 2020

Submitted to: *J. Phys.: Condens. Matter*

1. Introduction

The magnetic order can be excited by magnetic fields, spin [1, 2] and heat [3, 4] currents, mechanical rotations and sound waves [5, 6], optical fields in cavities [7, 8], and electric fields [9, 10, 11, 12, 13, 14]. A mechanism of the latter is *voltage-control of magnetic anisotropy* (VCMA), which avoids electric currents and thereby Joule heating. A time-dependent applied electric field can assist or fully actuate magnetization switching [12, 13, 14, 15, 16, 17, 18, 19, 20], and excite the ferromagnetic resonance [10, 12, 13, 14, 21]. However, in order to become useful, the VCMA should be enhanced. This can be realized by, for example, improving interface properties [22, 14], thermal stability [23], employing higher-order magnetic anisotropies [24], and reducing temperature dependences [25]. The control of magnetic properties by electric fields has also been demonstrated or proposed in magnetoelectric materials [26, 27, 28], by proximity effects [29, 30, 31], by nuclear spin resonance in single-molecule magnets [32], and by the tuning of exchange interactions [33, 34, 35, 36, 37, 38].

The electrostatic environment of a local moment affects its magnetic energy via the spin-orbit interaction (SOI) [39, 40]. In transition-metal atoms such as Fe, Co, and Ni with partially filled 3d subshells, the electrostatic interaction with neighboring atoms, $E_{CF} \sim 1$ eV is much larger than the SOI $E_{SOI} \sim 0.05$ eV [39], which implies that the orbital momentum of transition-metal ions is easily quenched, while the relatively large 3d orbital radius favors band formation and itinerant magnetism. The opposite occurs for the lanthanide series, i.e., atoms from lanthanum (La with atomic number 57) to lutetium (Lu with atomic number 71). The *rare earths* (RE) also include non-magnetic scandium (Sc) and yttrium (Y). The ground states of the lanthanide La^{+3} , Eu^{+3} , and Lu^{+3} ions are also not magnetic. The half-filled subshell of the magnetic ion Gd^{+3} lacks orbital angular momentum and, therefore, SOI. Except for La^{+3} , Eu^{+3} , Gd^{+3} , and Lu^{+3} , the 4f SOI energy of the lanthanide series $E_{SOI} \sim 0.2$ eV is much stronger than crystal-field energies $E_{CF} \sim 0.01$ eV [39], so their orbital momenta are atomic-like and not quenched. The magnetism of lanthanide-containing compounds can be understood by models that proceed from an atomic picture. Nevertheless, since the crystal fields lock to their spin-orbit induced anisotropic charge distributions, large magnetocrystalline anisotropies can be achieved.

The mechanism for the VCMA of RE moments is the electric field-induced torque on an anisotropic 4f charge distribution with rigidly coupled magnetic moment by the electric quadrupolar coupling [41]. This torque is communicated to the magnetic order via the exchange interaction.

Here, we predict that an interfacial RE dusting of transition-metal magnetic tunnel junctions can enhance its VCMA efficiency. We study the temperature dependence of the VCMA of RE moments, as well as the role of higher-order anisotropy constants. The latter issue has been addressed in transition-metal systems [24, 25], where the first- and second-order contributions partially cancel in the total VCMA. We calculate the magnetic anisotropy constants (MACs) of a rare-earth ion in the presence of an electric field, assuming a strong exchange coupling with the system magnetization. The effect is strongest for a RE at an interface between a magnetic metal and a non-magnetic insulator, such as $\text{Co}|\text{MgO}$. The Hamiltonian of the local moment in an angular momentum basis leads to so-called Stevens operators that can be easily diagonalized. We extract the intrinsic and field-induced MACs from the corresponding temperature-dependent free energy as a function of temperature.

2. Single-ion magnetic anisotropy

The 4f atomic radius is small compared to that of other filled atomic shells, which isolates the 4f electrons from other atoms in compounds [42]. Consequently, the crystal fields that would quench the orbital momentum of 3d transition metals only slightly affect 4f electron ground-state configurations. The 4f subshell is characterized by a spin (\mathbf{S}), an orbital momentum (\mathbf{L}), and a total angular momentum ($\mathbf{J} = \mathbf{L} + \mathbf{S}$). In the basis $|S, L, J, J_z\rangle$,

$$\mathbf{S}^2 |S, L, J, J_z\rangle = \hbar^2 S(S+1) |S, L, J, J_z\rangle,$$

$$\mathbf{L}^2 |S, L, J, J_z\rangle = \hbar^2 L(L+1) |S, L, J, J_z\rangle,$$

$$\mathbf{J}^2 |S, L, J, J_z\rangle = \hbar^2 J(J+1) |S, L, J, J_z\rangle,$$

$$\hat{J}_z |S, L, J, J_z\rangle = \hbar J_z |S, L, J, J_z\rangle,$$

where S and L are governed by Hund's first and second rules, respectively. The third rule determines the multiplet $J = L \pm S$, where the $-$ and $+$ is for the light (i.e., less than half-filled 4f shell with an atomic number less than 64) and heavy REs, respectively. We list the S , L , and J for the whole 4f series in table 1. In the following, we focus on the ground-state manifold with constant S , L , and J numbers. This multiplet of $J = L \pm S$ has $2J+1$ states that are degenerate in the absence of electromagnetic fields. Also,

$$\mathbf{S} = (g_J - 1)\mathbf{J},$$

$$\mathbf{L} = (2 - g_J)\mathbf{J},$$

$$\mathbf{L} + 2\mathbf{S} = g_J\mathbf{J},$$

where $g_J = 3/2 + [S(S+1) - L(L+1)]/[2J(J+1)]$ is the Landé g -factor. The projections of \mathbf{S} , \mathbf{L} , and $\mathbf{L} + 2\mathbf{S}$ on \mathbf{J} for lanthanide atoms manifests itself also in the crystal-field Hamiltonian, as shown in the next subsection.

| Ion | $4f^n$ | S | L | J | g_J |
|------------------|-----------|-----|---|------|-------|
| Ce ³⁺ | $4f^1$ | 1/2 | 3 | 5/2 | 6/7 |
| Pr ³⁺ | $4f^2$ | 1 | 5 | 4 | 4/5 |
| Nd ³⁺ | $4f^3$ | 3/2 | 6 | 9/2 | 8/11 |
| Pm ³⁺ | $4f^4$ | 2 | 6 | 4 | 3/5 |
| Sm ³⁺ | $4f^5$ | 5/2 | 5 | 5/2 | 2/7 |
| Eu ³⁺ | $4f^6$ | 3 | 3 | 0 | - |
| Gd ³⁺ | $4f^7$ | 7/2 | 0 | 7/2 | 2 |
| Tb ³⁺ | $4f^8$ | 3 | 3 | 6 | 3/2 |
| Dy ³⁺ | $4f^9$ | 5/2 | 5 | 15/2 | 4/3 |
| Ho ³⁺ | $4f^{10}$ | 2 | 6 | 8 | 5/4 |
| Er ³⁺ | $4f^{11}$ | 3/2 | 6 | 15/2 | 6/5 |
| Tm ³⁺ | $4f^{12}$ | 1 | 5 | 6 | 7/6 |
| Yb ³⁺ | $4f^{13}$ | 1/2 | 3 | 7/2 | 8/7 |

Table 1. Ground-state manifold of the tri-positive 4f ions. S , L , and J are the quantum numbers associated with \mathbf{S}^2 , \mathbf{L}^2 , and \mathbf{J}^2 , respectively. g_J is the Landé g-factor.

2.1. Stevens operators

Let us consider a crystal site with a potential that is invariant to rotations around the z -axis, which can be expanded as

$$-eV(\mathbf{r}) = A_2^{(0)}(3z^2 - r^2) + A_4^{(0)}(35z^4 - 30r^2z^2 + 3r^4) + A_6^{(0)}(231z^6 - 315z^4r^2 + 105z^2r^4 - 5r^6),$$

where $A_l^{(0)}$ is a *uniaxial crystal-field parameter* associated to the Y_l^0 spherical harmonic function (see Appendix A), usually expressed in units of temperature divided by a_0^l , where $a_0 \approx 0.53 \text{ \AA}$ is the Bohr radius. For example, for the 4f states of Nd₂Fe₁₄B [43] $A_2^{(0)} = 304 \text{ K}/a_0^2$, $A_4^{(0)} = -15 \text{ K}/a_0^4$, and $A_6^{(0)} = -2 \text{ K}/a_0^6$. The crystal-field parameters of the 4f and 4g states of other members of the (RE)₂Fe₁₄B family can be found in Ref. [43].

The electrostatic Hamiltonian of N_{4f} electrons in the subspace Hilbert space can be expanded into

$$\begin{aligned} \sum_{j=1}^{N_{4f}} (3\hat{z}_j^2 - \hat{r}_j^2) &= \vartheta_2 \langle r^2 \rangle \hat{O}_2^{(0)}, \\ \sum_{j=1}^{N_{4f}} (35\hat{z}_j^4 - 30\hat{r}_j^2\hat{z}_j^2 + 3\hat{r}_j^4) &= \vartheta_4 \langle r^4 \rangle \hat{O}_4^{(0)}, \\ \sum_{j=1}^{N_{4f}} h(\hat{r}_j, \hat{z}_j) &= \vartheta_6 \langle r^6 \rangle \hat{O}_6^{(0)}, \end{aligned} \quad (1)$$

where $h(\hat{r}_j, \hat{z}_j) = 231\hat{z}_j^6 - 315\hat{z}_j^4\hat{r}_j^2 + 105\hat{z}_j^2\hat{r}_j^4 - 5\hat{r}_j^6$ and \hat{z}_j and \hat{r}_j are the operators of the z and the radial coordinates of the j -th electron, respectively. $\langle r^l \rangle$ is the mean value of r^l calculated for a 4f (atomic) radial wave function. The projection constants ϑ_l are listed in Table 2, while *Stevens equivalent operators* are $\hbar^2\hat{O}_2^{(0)} = 3\hat{J}_z^2 - \mathbf{J}^2$,

| Ion | $4f^n$ | $10^2\vartheta_2$ | $10^3\vartheta_4$ | $10^4\vartheta_6$ |
|------------------|-----------|-------------------|-------------------|-------------------|
| Ce ³⁺ | $4f^1$ | -5.71 | 6.35 | 0 |
| Pr ³⁺ | $4f^2$ | -2.10 | -0.73 | 0.61 |
| Nd ³⁺ | $4f^3$ | -0.64 | -0.29 | -0.38 |
| Pm ³⁺ | $4f^4$ | 0.77 | 0.41 | 6.69 |
| Sm ³⁺ | $4f^5$ | 4.13 | 2.50 | 0 |
| Eu ³⁺ | $4f^6$ | - | - | - |
| Gd ³⁺ | $4f^7$ | - | - | - |
| Tb ³⁺ | $4f^8$ | -1.01 | 0.12 | -0.01 |
| Dy ³⁺ | $4f^9$ | -0.63 | -0.06 | 0.01 |
| Ho ³⁺ | $4f^{10}$ | -0.22 | -0.03 | -0.01 |
| Er ³⁺ | $4f^{11}$ | 0.25 | 0.04 | 0.02 |
| Tm ³⁺ | $4f^{12}$ | 1.01 | 0.16 | -0.06 |
| Yb ³⁺ | $4f^{13}$ | 3.17 | -1.73 | 1.48 |

Table 2. Projection constants in the Stevens' operators Eqs. (1) [45]. The nearly ellipsoidal 4f electron density causes a hierarchy of projection constants, i.e., most ions obey the scaling $|\vartheta_2| \sim 10^{-3} - 10^{-2}$, $|\vartheta_4| \sim 10^{-5} - 10^{-3}$, and $|\vartheta_6| \sim 10^{-6} - 10^{-4}$, and then the quadrupole dominates. Some references use the notation $\alpha_J = \vartheta_2$, $\beta_J = \vartheta_4$, and $\gamma_J = \vartheta_6$.

$$\hbar^4\hat{O}_4^{(0)} = 35\hat{J}_z^4 - 30\mathbf{J}^2\hat{J}_z^2 + 25\hbar^2\hat{J}_z^2 - 6\hbar^2\mathbf{J}^2 + 3\mathbf{J}^4, \quad (3)$$

$$\begin{aligned} \hbar^6\hat{O}_6^{(0)} &= 231\hat{J}_z^6 - 315\mathbf{J}^2\hat{J}_z^4 + 735\hbar^2\hat{J}_z^4 + 105\mathbf{J}^4\hat{J}_z^2 \\ &\quad - 525\hbar^2\mathbf{J}^2\hat{J}_z^2 + 294\hbar^4\hat{J}_z^2 - 5\mathbf{J}^6 + 40\hbar^2\mathbf{J}^4 - 60\hbar^4\mathbf{J}^2. \end{aligned} \quad (4)$$

Stevens operators for other symmetries are listed in [44, 45, 46]. The total crystal-field Hamiltonian reads

$$H_{CF} = -e \sum_{j=1}^{N_{4f}} V(\mathbf{r}_j) = \sum_{l=2,4,6} \vartheta_l \langle r^l \rangle A_l^{(0)} \hat{O}_l^{(0)}. \quad (5)$$

2.2. Magnetic anisotropy constants

In several magnets, the exchange interaction strongly couples the 4f local moments to the magnetization $\mathbf{m} = \sin\theta(\cos\phi\mathbf{e}_x + \sin\phi\mathbf{e}_y) + \cos\theta\mathbf{e}_z$, where \mathbf{e}_j is the unit vector along the Cartesian axis j . Then, the Hamiltonian H of a single RE atom reads

$$H = H_{CF} + \frac{J_{ex}(g_J - 1)f(T)}{\hbar} \mathbf{J} \cdot \mathbf{m}, \quad (6)$$

where $J_{ex} > 0$ is the exchange constant with units of energy. The exchange coupling favors the parallel alignment between the magnetization \mathbf{m} and the spin contribution to the 4f moment $-\gamma_e(g_J - 1)\mathbf{J}$, with $-\gamma_e$ being the electron gyromagnetic ratio. Note that the 4f spin \mathbf{S} is antiparallel (parallel) to \mathbf{J} for the light (heavy) lanthanides because of $g_J < 1$ ($g_J > 1$). $f(T)$ parameterizes the temperature dependence of the system magnetization [47, 48]

$$f(T) = \left[1 - s \left(\frac{T}{T_C} \right)^{3/2} - (1 - s) \left(\frac{T}{T_C} \right)^p \right]^{1/3}, \quad (7)$$

where T_C is the Curie temperature, and s and p (2)(with $p > s$) are material-dependent parameters. For

example, for Co [47], $T_C = 1385$ K, $s = 0.11$, and $p = 5/2$; for Fe, $T_C = 1044$ K, $s = 0.35$, and $p = 4$. Empirical expression (7) describes the temperature dependence between Bloch's law $1 - (s/3)(T/T_C)^{3/2}$ for $T \rightarrow 0$ and the critical scaling $(1 - T/T_C)^{1/3}$ for $T \rightarrow T_C$. Equation (7) is all we need to know about the magnetic host.

The Helmholtz free energy [49]

$$F = -\frac{1}{\beta} \ln \left[\sum_{n=1}^{2J+1} e^{-\beta E_n} \right], \quad (8)$$

where $\beta = 1/(k_B T)$, $k_B = 8.617 \times 10^{-5}$ eV/K is Boltzmann's constant, T is temperature, and E_n is the n -th eigenvalue of Eq. (6). The uniaxial anisotropy energy density can be expanded in the magnetization direction θ as [39, 40]

$$n_{RE} F = K_1 \sin^2 \theta + K_2 \sin^4 \theta + K_3 \sin^6 \theta, \quad (9)$$

where n_{RE} is the (surface or volume) density of RE moments and

$$K_1 = \frac{n_{RE}}{2} \lim_{\theta \rightarrow 0} \left[(\partial_\theta)^2 F \right], \quad (10)$$

$$K_2 = \frac{n_{RE}}{4!} \lim_{\theta \rightarrow 0} \left[(\partial_\theta)^4 F \right] + \frac{K_1}{3}, \quad (11)$$

$$K_3 = \frac{n_{RE}}{6!} \lim_{\theta \rightarrow 0} \left[(\partial_\theta)^6 F \right] - \frac{2K_1}{45} + \frac{2K_2}{3}, \quad (12)$$

are the magnetic anisotropy constants (MACs) and $(\partial_\theta)^m$ is the m -th order partial derivative with respect to θ .

F and the MACs depend on the eigenenergies E_n of the 4f Hamiltonian, Eq. (6), by Eqs. (8) and (10-12). For example, when $J = 1$ and in the limit of large exchange ($|J_{ex}| \gg |\partial_l \langle r^l \rangle A_l^{(0)}|$, for $l = 2, 4, 6$) and low temperatures ($k_B T \rightarrow 0$),[‡]

$$K_1 = -\frac{3}{2} n_{RE} \theta_2 \langle r^2 \rangle A_2^{(0)}. \quad (13)$$

K_1 does not depend on the exchange constant [49]. Equation (13) is consistent with Ref. [40] and can be written as $K_1/n_{RE} = -(3/2)Q_2 A_2^{(0)}$, where $Q_2 = \theta_2 \langle r^2 \rangle$ is the quadrupolar moment for $J_z = J = 1$, a measure of the asphericity of the 4f subshell charge density.

The calculation of general MACs requires the diagonalization of a $(2J + 1)$ times $(2J + 1)$ matrix. An analytic calculation of K_1 , K_2 and K_3 for arbitrary temperature and exchange constants is tedious, but easily carried out numerically.

In the following, we numerically compute the temperature-dependent MACs induced by electric fields at an *insulator|metal* interface, also considering that crystal fields at interfaces may substantially differ from that in bulk crystals. We assume

[‡] Some denote the magnetic anisotropy energy as $\kappa_1 \cos^2 \theta$ instead of $K_1 \sin^2 \theta$ with $\kappa_1 = -K_1$.

uniaxial symmetry and denote the interface crystal field parameters by $\bar{A}_l^{(0)}$. An applied voltage can give rise to locally large electric fields E_0 normal to a metal|insulator interface (along the z -axis), which contributes as $\Delta A_l^{(0)}$ with total $\tilde{A}_l^{(0)} = \bar{A}_l^{(0)} + \Delta A_l^{(0)}$.

3. Electric field-dependent magnetic anisotropy

The applied electric field E_0 is screened on the scales of the Thomas-Fermi length $d_{TF} \sim 1$ Å on the metal side, so $\mathbf{E} = E_0 e^{-z/d_{TF}} \mathbf{e}_z$ for $z > 0$, with $z = 0$ being the interface position. Close to $z = 0$ and using the expressions from Appendix A,

$$\Delta A_2^{(0)} = -\frac{eE_0}{6d_{TF}}, \quad (14)$$

$$\Delta A_4^{(0)} = -\frac{eE_0}{840d_{TF}^3}, \quad (15)$$

$$\Delta A_6^{(0)} = -\frac{eE_0}{166320d_{TF}^5}. \quad (16)$$

Therefore, the electric field modifies not only the second-order uniaxial anisotropy but also higher-order terms. With this set of crystal-field parameters, we can diagonalize the atomic Hamiltonian (6), evaluate the free energy (8), and the MACs (10-12), see Appendix B. We plot the spectra E_n with $n \in \{1, \dots, 2J + 1\}$ at room temperature in Fig. 1 in units of the thermal energy for $J_{ex} = 0.1$ eV, $E_0 = 10$ mV/nm, and $\theta = 0$. The exchange interaction dominates the term splittings, while electric-field effects are small.

The MACs ΔK_l from $\Delta A_l^{(0)}$ are proportional to the applied electric field E_0 . ΔK_1 has a negative slope for the oblate (pancake-shaped) ions Ce^{3+} , Pr^{3+} , Nd^{3+} , Tb^{3+} , Dy^{3+} , and Ho^{3+} , and a positive slope for the prolate (cigar-shaped) ions Pm^{3+} , Sm^{3+} , Er^{3+} , Tm^{3+} , and Yb^{3+} , consistent with previous results [41]. Figure 2 shows the VCMA contributions of a set of

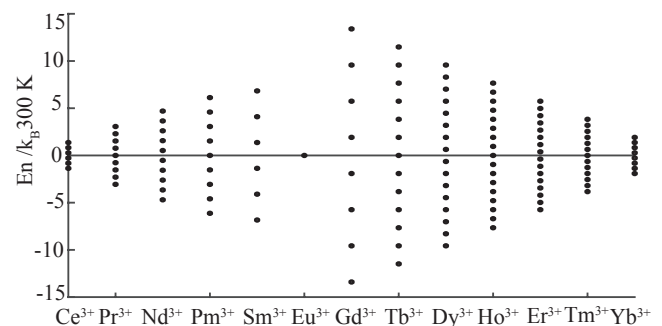


Figure 1. Energy spectra of lanthanide local moments at a Co surface at room temperature, in units of $300 K k_B$, $J_{ex} = 0.1$ eV, $E_0 = 10$ mV/nm, and magnetization along z (i.e., $\theta = 0$). Crystal-electric field effects are not included. The dots are the calculated eigenvalues E_n of the Hamiltonian (6).

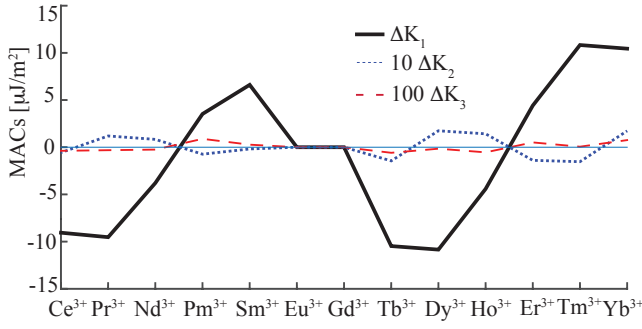


Figure 2. Voltage-controlled magnetic anisotropy (MAC) per unit of electric field E_0 , $\Delta K_1/E_0$ (solid line), $\Delta K_2/E_0$ (square-dashed line) and $\Delta K_3/E_0$ (dashed line) of rare earth moments at the surface of Co at low temperatures ($T = 0.01$ mK). Here we use the density $n_{RE} = 1/\text{nm}^2$ and exchange constant $J_{ex} = 0.1$ eV. For better visibility, ΔK_2 and ΔK_3 are enlarged by a factor of 10 and 100, respectively. For an electric field $E_0 = 10$ mV/nm = 100 kV/cm, ΔK_1 is of the order $\mu\text{J}/\text{m}^2$ for most lanthanides.

RE atoms at an interface at low temperatures with $n_{RE} = 1 \text{ nm}^{-2}$, and $J_{ex} = 0.1$ eV. We use $d_{TF} = 1 \text{ \AA}$ and the Co parameters for the magnetization, $\{T_c, s, p\} = \{1385 \text{ K}, 0.11, 5/2\}$ in Eq. (7), assuming that they are not affected much by the interface. The MACs in units of energy density result from dividing the surface MACs by the thickness of the magnetic film. For example, dusting the interface with one Tm^{+3} ion per nm^2 with a field of $E_0 \sim 1 \text{ V/nm} = 10^4 \text{ kV/cm}$ creates an energy volume density of $1 \text{ MJ}/\text{m}^3$ in a 1 nm-thick Co film. Figure 2 illustrates that the VCMA of rare earths is governed only by K_1 , while K_2 and K_3 are negligibly small. This hierarchy differs from that of transition metals, where K_1 and K_2 are of the same order of magnitude and partially compensate each other [24, 25]. This difference can be understood as follows. The l -th order MAC divided by the characteristic electrostatic energy, $eE_0 d_{TF}$, scales as $\Delta K_j / (eE_0 d_{TF}) \propto \vartheta_{2j} \langle r^{2j} \rangle / d_{TF}^{2j}$. The 4f subshell envelope is nearly ellipsoidal, which is accounted for by the hierarchy of the projections constants $|\vartheta_2| \ll |\vartheta_4| \ll |\vartheta_6|$. The transition metal 3d shells are more polarizable and can be more easily deformed by the crystal fields than the lanthanides. A consequence is that the quadrupole contribution of the voltage-controlled anisotropy ΔK_1 of rare earths is much larger than ΔK_2 and ΔK_3 .

The temperature dependence of rare-earth magnetic anisotropies in bulk materials has been extensively studied [39, 40, 48]. Here we calculate the temperature dependence of the VCMA-efficiency for rare-earth atoms at an interface between a non-magnetic insulator (such as MgO) and a magnetic metal, such as Fe or Co. Figure 3 illustrates the temperature-dependence of K_1/E_0 for all lanthanides with a finite orbital momentum in the temperature range $0 \text{ K} \leq T \leq 1400$

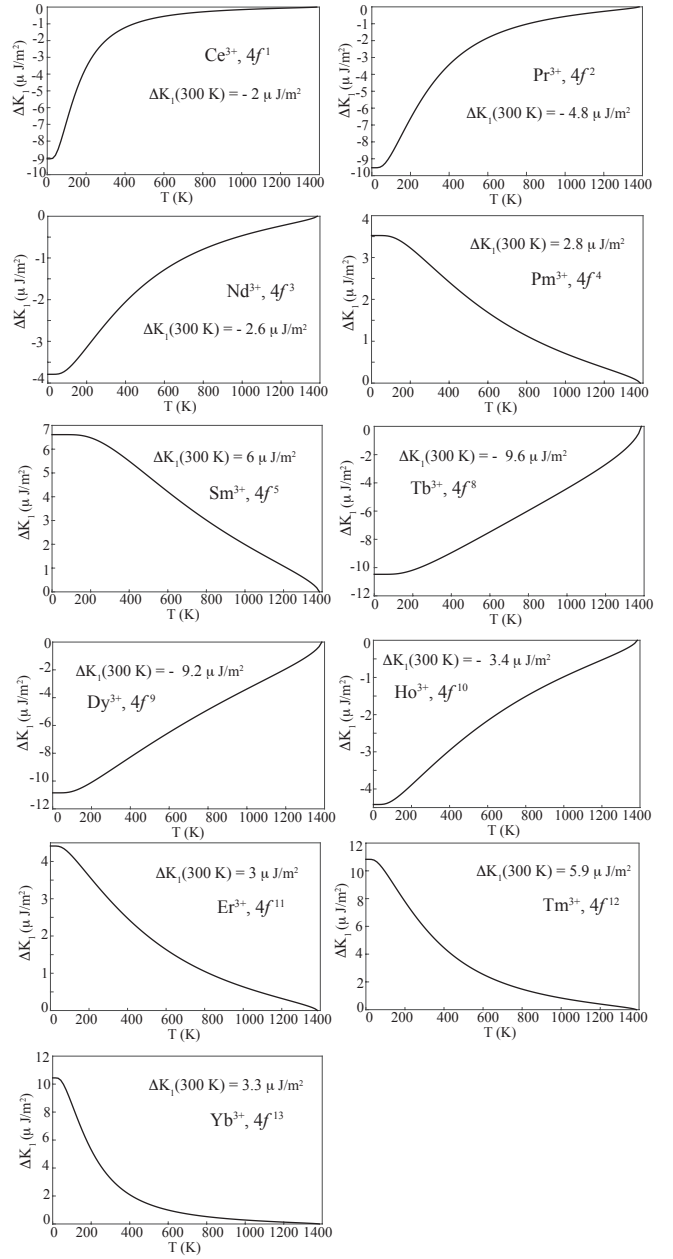


Figure 3. Magnetic anisotropy constants per unit of electric field, $\Delta K_1/E_0$, as a function of temperature for a rare-earth density $n_{4f} = 1/\text{nm}^2$ at a Co surface.

K for $n_{RE} = 1 \text{ nm}^{-2}$. K_1 at room temperature, $T = 300 \text{ K}$, is specified inside each graph. The efficiency at room-temperature is largest for Tb^{3+} and Dy^{3+} with $\Delta K_1/E_0 = -960 \text{ fJ/Vm}$ and $\Delta K_1/E_0 = -910 \text{ fJ/Vm}$, respectively. For an applied field of $E_0 = 10 \text{ mV/nm}$, the corresponding VCMA values of Tb^{3+} and Dy^{3+} are $\Delta K_1 = -9.6 \mu\text{J}/\text{m}^2$ and $\Delta K_1 = -9.1 \mu\text{J}/\text{m}^2$.

In the absence of exchange coupling between the 4f angular momentum (\mathbf{J}) and the magnetization (\mathbf{m}), REs do not contribute to the anisotropy, so the VCMA

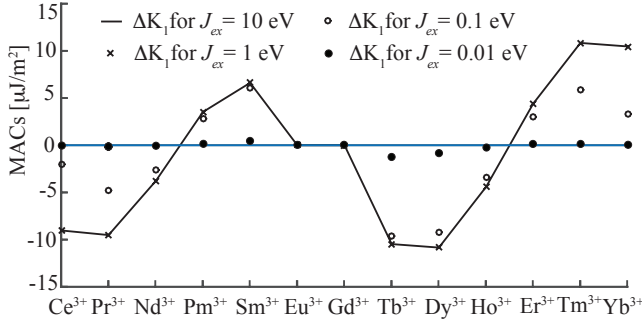


Figure 4. Magnetic anisotropy constant per unit of electric field, $\Delta K_1/E_0$, for exchange constants $J_{ex} = 10$ eV (solid line), $J_{ex} = 1$ eV (crosses), $J_{ex} = 0.1$ eV (open circles), and $J_{ex} = 0.01$ eV (full circles). This graph uses $T = 300$ K and a density $n_{Af} = 1/\text{nm}^2$ at a Co surface. The thin horizontal line $\Delta K_1/E_0 = 0$ is just for visual guidance.

strength vanishes for $J_{ex} \rightarrow 0$. This tendency is shown in Fig. 4 for $0.01 \text{ eV} \leq J_{ex} \leq 10 \text{ eV}$ at $T = 300$ K. Results are not very sensitive to the value of typical exchange constants, $0.1 \text{ eV} \leq J_{ex} < 1 \text{ eV}$, as long as they are larger than the anisotropy induced by the crystal fields or applied voltages ($\sim 0.01 \text{ eV}$ [39]).

4. Intrinsic interface magnetic anisotropy

The intrinsic (i.e., at zero applied electric field) magnetic anisotropy at the interface cannot be calculated accurately in an easy way. Simple approaches, such as the point-charge model, are not adequate for metals due to the efficient screening by conduction electrons [50]. The screened-charge model of metals [50] can characterize interfacial anisotropies in metallic multilayers [51]. However, this model is not valid for metal|insulator interfaces with a nearly discontinuous conduction electron density.

Here we estimate the order of magnitude of the intrinsic interfacial RE magnetic anisotropy by the model of a local moment in a metal at the origin surrounded by four oxygen atoms with Cartesian coordinates $(\pm d_{ox}, 0, -d_{ox})/\sqrt{2}$ and $(0, \pm d_{ox}, -d_{ox})/\sqrt{2}$ and five transition-metal atoms (such as Co or Fe) at positions $(\pm d_{TM}, 0, 0)$, $(0, \pm d_{TM}, 0)$ and $(0, 0, d_{TM})$, as shown in Fig. 5. The uniaxial crystal-field parameter [39, 40, 50] reads

$$\bar{A}_2^{(0)} = \sum_j \frac{A'_j}{2} (3 \cos^2 \theta_j - 1),$$

where j labels the ligand, $\cos \theta_j$ is the z -component of the j -th site position (\mathbf{r}_j), and A'_j depends on the distance $d_j = |\mathbf{r}_j|$

$$A'_j(d_j) = -\frac{eQ_j}{4\pi\epsilon_0} \frac{e^{-d_j/d_{TF}}}{2d_j^3} \left[1 + \frac{d_j}{d_{TF}} + \frac{1}{3} \left(\frac{d_j}{d_{TF}} \right)^2 \right],$$

where ϵ_0 is the vacuum permittivity. We adopt the screened charges [50] approach for $Q_j = Q_j(d_{TF})$. For $d_{ox} = 6 \text{ \AA}$, $d_{TM} = 5 \text{ \AA}$, and $d_{TF} = 1 \text{ \AA}$, and A'_j/k_B for iron and oxygen of the order of magnitude of 100 Ka_0^{-2} and 200 Ka_0^{-2} , respectively, $\bar{A}_2^{(0)} \sim 3 \times 10^{18} \text{ eV/m}^2$ is of the same order as that produced by an electric field of $E_0 = -1.8 \text{ V/nm}$.

For the present interface model, oblate (prolate) ions with $\vartheta_2 < 0$ ($\vartheta_2 > 0$) favor a perpendicular (in-plane) magnetization. Doping a transition-metal layer with oblate rare-earth ions enhances the perpendicular interface anisotropy, which is important for spin transfer torque magnetic random-access memories (STT-MRAM), but also implies need for higher voltages to achieve VCMA-induced magnetization switching. In transition metals, on the other hand, the intrinsic magnetic anisotropies are small, and electric-field effects easily dominate. A quantitative description of the intrinsic interface rare-earth anisotropy as a function of interface structure and morphology requires first-principles calculations.

5. Conclusions and discussion

We studied the temperature-dependent *voltage-controlled magnetic anisotropy* of rare-earth atoms at a magnetic metal|non-magnetic insulator interface. Our findings differ from the conventional wisdom based on transition metals. In rare earths, only the lowest-order uniaxial constant can be efficiently modulated by a voltage because of the small 4f radius and rigid ellipsoidal shape of the 4f shell electron density. To leading order, the magnetic anisotropy constants change linearly with the applied electric field, with a negative slope for the oblate (pancake-like) Ce^{3+} , Pr^{3+} , Nd^{3+} , Tb^{3+} , Dy^{3+} , and Ho^{3+} , and a positive one for the prolate Pm^{3+} , Sm^{3+} , Er^{3+} , Tm^{3+} , and Yb^{3+} moments. Rare earths at an interface also contribute to the in-

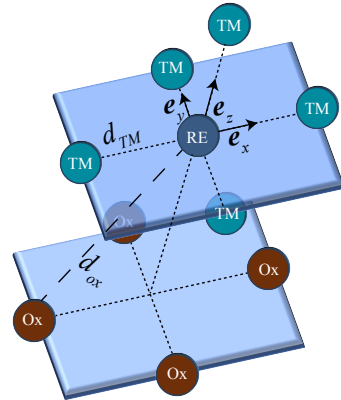


Figure 5. Sketch of the ligands of a RE atom at a metal|insulator interface.

trinsic (i.e., independent of the applied electric field) magnetic anisotropy, the oblate (prolate) ones favoring a perpendicular (in-plane) equilibrium magnetization.

Our model assumes metallic screening, i.e., a drop of the electric field over atomic distances at the interface which hosts the rare earth moments. This assumption might break down at non-ideal interfaces, so it should be confirmed by experimental or ab initio methods.

Nevertheless, we are confident about substantial effects at room temperature for even low densities of RE atoms ($\sim 1/\text{nm}^2$). Since the electric field is strongly enhanced at metal|insulator interfaces, bulk doping of a magnet with rare earths is not efficient. Still, the dusting of the interface between a tunnel barrier and a transition metal thin film can significantly enhance the switching efficiency of voltage-controlled tunnel junctions.

Acknowledgments

This research was supported by JSPS KAKENHI Grant No. 19H006450, Postdoctorado FONDECYT 2019 Folio 3190030, and Financiamiento Basal para Centros Científicos de Excelencia FB0807.

Appendix A. Expansion into spherical harmonics

We focus on the axially symmetric potentials, $-eV(\mathbf{r})$, that we decompose into the Spherical harmonics $Y_l^0(\theta)$

$$Y_l^0(\theta) = \sqrt{\frac{2l+1}{4\pi}} P_l(\cos\theta), \quad (\text{A.1})$$

where $l = 2, 4, 6$ and P_l is the l -th Legendre polynomial,

$$P_2(x) = \frac{1}{2}(3x^2 - 1), \quad (\text{A.2})$$

$$P_4(x) = \frac{1}{8}(35x^4 - 30x^2 + 3), \quad (\text{A.3})$$

$$P_6(x) = \frac{1}{16}(231x^6 - 315x^4 + 105x^2 - 5). \quad (\text{A.4})$$

leading to a multipolar expansion up to the 6th order in r

$$\begin{aligned} -eV(\mathbf{r}) = & 4\sqrt{\frac{\pi}{5}}Y_2^0(\theta)r^2A_2^{(0)} + 16\sqrt{\frac{\pi}{9}}Y_4^0(\theta)r^4A_4^{(0)} \\ & + 32\sqrt{\frac{\pi}{13}}Y_6^0(\theta)r^6A_6^{(0)} + c_0(\theta), \end{aligned} \quad (\text{A.5})$$

where $c_0(\theta)$ collects the odd terms in z (dipolar-like contributions) that do not interact with a nearly ellipsoidal 4f subshell (i.e., the fields are not large enough to polarize/asymmetrize the subshell). Using the orthonormality of spherical harmonic functions, $\int_0^\pi d\theta \sin\theta \int_0^{2\pi} d\phi [Y_{l'}^{m'}(\theta, \phi)]^* Y_l^m(\theta, \phi) = \delta_{l,l'}\delta_{m,m'}$,

one gets

$$A_2^{(0)} = \frac{-e}{4r^2} \sqrt{\frac{5}{\pi}} \int_0^\pi d\theta \sin\theta \int_0^{2\pi} d\phi Y_2^0(\theta) V(\mathbf{r}), \quad (\text{A.6})$$

$$A_4^{(0)} = \frac{-e}{16r^4} \sqrt{\frac{9}{\pi}} \int_0^\pi d\theta \sin\theta \int_0^{2\pi} d\phi Y_4^0(\theta) V(\mathbf{r}), \quad (\text{A.7})$$

$$A_6^{(0)} = \frac{-e}{32r^6} \sqrt{\frac{13}{\pi}} \int_0^\pi d\theta \sin\theta \int_0^{2\pi} d\phi Y_6^0(\theta) V(\mathbf{r}). \quad (\text{A.8})$$

The single-electron 4f wave functions have principal and orbital quantum numbers $n = 4$ and $l = 3$, respectively. Consequently, the 4f charge distribution has non-vanishing multipoles up to the $2l = 6$ -th order.

Appendix B. Numerical Details

For convenience, we introduce dimensionless parameters for the MACs $k_i \equiv \Delta K_i / (n_{RE} J_{ex})$, reciprocal thermal energy $\bar{\beta} \equiv J_{ex} \beta$, and crystal-field parameters $a_l \equiv \vartheta_l \langle r^l \rangle A_l^{(0)} / J_{ex}$. The reduced Helmholtz free energy $F/J_{ex} = -\bar{\beta}^{-1} \ln \sum e^{-\bar{\beta} \epsilon_n}$, where $\epsilon_n \equiv E_n / J_{ex}$ is the n -th eigenvalue of the dimensionless 4f Hamiltonian H/J_{ex} . We approximate the radial 4f wave function by a Slater-type orbital, $R(r) \propto r^3 e^{-r/a}$, with $a = 0.133 \text{ \AA}$, such that the mean value $\langle r \rangle = 0.6 \text{ \AA}$ [42]. Then, $\langle r^2 \rangle = 0.4 \text{ \AA}^2$, $\langle r^4 \rangle = 0.24 \text{ \AA}^4$, and $\langle r^6 \rangle = 0.19 \text{ \AA}^6$. We use the T_C , s and p values of Co for the temperature dependence of the host magnetization [47]. The derivatives of Eqs. (10), (11), and (12) are discretized using central schemes of order $\Delta\theta^2$, with the θ step-size $\Delta\theta = 0.1$. A finer grid $\Delta\theta = 0.05$ and $\Delta\theta = 0.01$ leads to the same results.

- [1] Ralph D C and Stiles M D 2008 Spin transfer torques *J. Magn. Magn. Mater.* **320** 1190
- [2] Avci C O, Quindeau A, Pai C-F, Mann M, Caretta L, A, Tang A S, Onbasli M C, Ross C A and Beach G S D 2017 Current-induced switching in a magnetic insulator *Nat. Mater.* **16** 309
- [3] Bauer G E W, Saitoh E and van Wees B J 2012 Spin caloritronics *Nat. Mater.* **11** 391
- [4] Otani Y, Shiraishi M, Oiwa A, Saitoh E and Murakami S 2017 Spin conversion on the nanoscale *Nat. Phys.* **13** 829
- [5] Matsuo M, Ieda J, Saitoh E and Maekawa S 2011 Spin current generation due to mechanical rotation in the presence of impurity scattering *Appl. Phys. Lett.* **98** 242501
- [6] Kobayashi D, Yoshikawa T, Matsuo M, Iguchi R, Maekawa S, Saitoh E and Nozaki Y 2017 Spin Current Generation Using a Surface Acoustic Wave Generated via Spin-Rotation Coupling *Phys. Rev. Lett.* **119** 077202
- [7] Zhang X, Zou C-L, Jiang L and Tang H X 2014 Strongly Coupled Magnons and Cavity Microwave Photons *Phys. Rev. Lett.* **113** 156401
- [8] Yu W, Wang J, Yuan H Y and Xiao J 2019 Prediction of Attractive Level Crossing via a Dissipative Mode *Phys. Rev. Lett.* **123** 227201
- [9] Suzuki Y, Kubota H, Tulapurkar A and Nozaki T 2011 Spin control by application of electric current and voltage in FeCoMgO junctions *Phil. Trans. R. Soc. A* **369** 3658
- [10] Nozaki T, Shiota Y, Miwa S, Murakami S, Bonell F, Ishibashi S, Kubota H, Yakushiji K, Saruya T,

- Fukushima A, Yuasa S, Shinjo T and Suzuki Y 2012 Electric-field-induced ferromagnetic resonance excitation in an ultrathin ferromagnetic metal layer *Nat. Phys.* **8** 491
- [11] Verba R, Tiberkevich V, Krivorotov I and Slavin A 2014 Parametric Excitation of Spin Waves by Voltage-Controlled Magnetic Anisotropy *Phys. Rev. Appl.* **1** 044006
- [12] Matsukura F, Tokura Y and Ohno H 2015 Control of magnetism by electric fields *Nat. Nano.* **10** 209
- [13] Song C, Cui B, Li F, Zhou X and Pan F 2017 Recent progress in voltage control of magnetism: Materials, mechanisms, and performance *Prog. Mater.* **87** 33
- [14] Nozaki T, Yamamoto T, Miwa S, Tsujikawa M, Shirai M, Yuasa S and Suzuki Y 2019 Recent Progress in the Voltage-Controlled Magnetic Anisotropy Effect and the Challenges Faced in Developing Voltage-Torque MRAM *Micromachines* **10** 327
- [15] Shiota Y, Maruyama T, Nozaki T, Shinjo T, Shirai M and Suzuki Y 2009 Voltage-Assisted Magnetization Switching in Ultrathin Fe₈₀Co₂₀ Alloy Layers *Appl. Phys. Express* **2** 063001
- [16] Shiota Y, Nozaki T, Bonell F, Murakami S, Shinjo T and Suzuki T 2012 Induction of coherent magnetization switching in a few atomic layers of FeCo using voltage pulses *Nat. Mater.* **11** 39
- [17] Wang W-G, Li M, Hageman S and Chien CL 2012 Electric-field-assisted switching in magnetic tunnel junctions *Nat. Mater.* **11** 64
- [18] Kanai S, Yamanouchi M, Ikeda S, Nakatani Y, Matsukura F and Ohno H 2012 Electric field-induced magnetization reversal in a perpendicular-anisotropy CoFeB-MgO magnetic tunnel junction *Appl. Phys. Lett.* **101** 122403
- [19] Kanai S, Matsukura F and Ohno H 2016 Electric-field-induced magnetization switching in CoFeB/MgO magnetic tunnel junctions with high junction resistance *Appl. Phys. Lett.* **108**, 192406
- [20] Grezes C, Ebrahimi F, Alzate J G, Cai X, Katine J A, Langer J, Ocker B, Amiri P K and Wang K L 2016 Ultra-low switching energy and scaling in electric-field-controlled nanoscale magnetic tunnel junctions with high resistance-area product *Appl. Phys. Lett.* **108**, 012403
- [21] Zhu J, Katine J A, Rowlands G E, Chen Y J, Duan Z, Alzate J G, Upadhyaya P, Langer J, Amiri P K, Wang K L and Krivorotov I N 2012 Voltage-Induced Ferromagnetic Resonance in Magnetic Tunnel Junctions *Phys. Rev. Lett.* **108** 197203
- [22] Wen Z, Sukegawa H, Seki T, Kubota T, Takanashi K and Mitani S 2017 Voltage control of magnetic anisotropy in epitaxial Ru/Co₂FeAl/ MgO heterostructures *Sci. Rep.* **7** 45026
- [23] Shiota Y, Nozaki T, Tamaru S, Yakushiji K, Kubota H, Fukushima A, Yuasa S and Suzuki Y 2017 Reduction in write error rate of voltage-driven dynamic magnetization switching by improving thermal stability factor *Appl. Phys. Lett.* **111** 022408
- [24] Sugihara A, Nozaki T, Kubota H, Imamura H, Fukushima A, Yakushiji K and Yuasa S 2019 Evaluation of higher order magnetic anisotropy in a perpendicularly magnetized epitaxial ultrathin Fe layer and its applied voltage dependence *Jpn. J. Appl. Phys.* **58** 090905
- [25] Sugihara A, Spiesser A, Nozaki T, Kubota H, Imamura H, Fukushima A, Yakushiji K and Yuasa S 2020 Temperature dependence of higher-order magnetic anisotropy constants and voltage-controlled magnetic anisotropy effect in a Cr/Fe/MgO junction *Jpn. J. Appl. Phys.* **59** 010901
- [26] Gerhard L, Yamada T K, Balashov T, Takács A F, Wesselink R J H, Däne M, Fechner M, Ostanin S, Ernst A, Mertig I and Wulfhekel W 2010 Magnetolectric coupling at metal surfaces *Nat. Nano.* **5** 792
- [27] Yamada Y, Ueno K, Fukumura T, Yuan H T, Shimotani H, Iwasa Y, Gu L, Tsukimoto S, Ikuhara Y and Kawasaki M 2011 Electrically Induced Ferromagnetism at Room Temperature in Cobalt-Doped Titanium Dioxide *Science* **332** 1065
- [28] Sekine A and Chiba T 2016 Electric-field-induced spin resonance in antiferromagnetic insulators: Inverse process of the dynamical chiral magnetic effect *Phys. Rev. B* **93** 220403(R)
- [29] Miwa S, Suzuki M, Tsujikawa M, Matsuda K, Nozaki T, Tanaka K, Tsukahara T, Nawaoka K, Goto M, Kotani Y, Ohkubo T, Bonell F, Tamura E, Hono K, Nakamura T, Shirai M, Yuasa S and Suzuki Y 2017 Voltage controlled interfacial magnetism through platinum orbits *Nat. Comm.* **8** 15848
- [30] Liang L, Shan J, Chen Q H, Lu J M, Blake G R, Palstra T T M, Bauer G E W, van Wees B J and Ye J T 2018 Gate-controlled magnetoresistance of a paramagnetic-insulator—platinum interface *Phys. Rev. B* **98** 134402
- [31] Takiguchi K, Anh L D, Chiba T, Koyama T, Chiba D and Tanaka M 2019 Giant gate-controlled proximity magnetoresistance in semiconductor-based ferromagnetic/non-magnetic bilayers *Nat. Phys.* **15** 1134
- [32] Thiele S, Balestro F, Ballou R, Klyatskaya S, Ruben M and Wernsdorfer W 2014 Electrically driven nuclear spin resonance in single-molecule magnets *Science* **344** 6188
- [33] You C-Y and Suzuki Y 2005 Tunable interlayer exchange coupling energy by modification of Schottky barrier potentials *J. Magn. Magn. Mater.* **293** 774
- [34] Haney P M, Heiliger C and Stiles M D 2009 Bias dependence of magnetic exchange interactions: Application to interlayer exchange coupling in spin valves *Phys. Rev. B* **79** 054405
- [35] Tang Y-H, Kioussis N, Kalitsov A, Butler W H and Car R 2009 Controlling the Nonequilibrium Interlayer Exchange Coupling in Asymmetric Magnetic Tunnel Junctions *Phys. Rev. Lett.* **103** 057206
- [36] Newhouse-Ilige T, Liu Y, Xu M, Hickey D R, Kundu A, Almasi H, Bi C, Wang X, Freeland J W, Keavney D J, Sun C J, Xu Y H, Rosales M, Cheng X M, Zhang S, Mkhoyan K A and Wang W G 2017 Voltage-controlled interlayer coupling in perpendicularly magnetized magnetic tunnel junctions *Nat. Comm.* **8** 15232
- [37] Yang Q, Wang L, Zhou Z, Wang L, Zhang Y, Zhao S, Dong G, Cheng Y, Min T, Hu Z, Chen W, Xia K and Liu M 2018 Ionic liquid gating control of RKKY interaction in FeCoB/Ru/FeCoB and (Pt/Co)₂/Ru/(Co/Pt)₂ multilayers *Nat. Comm.* **9** 991
- [38] Leon A O, d'Albuquerque e Castro J, Retamal J C, Cahaya A B and Altbir D 2019 Manipulation of the RKKY exchange by voltages *Phys. Rev. B* **100** 014403
- [39] Skomski R 2008 *Simple Models of Magnetism* (Oxford University Press)
- [40] Skomski R and Coey J M D 1999 *Permanent Magnetism* (Institute of Physics Publishing)
- [41] Leon A O, Cahaya A B and Bauer G E W 2018, Voltage Control of Rare-Earth Magnetic Moments at the Magnetic-Insulator-Metal Interface *Phys. Rev. Lett.* **120** 027201
- [42] Jensen J and Mackintosh A R 1991 *Rare Earth Magnetism* (Oxford: Clarendon Press)
- [43] Coey J M D (ed) 1996 *Rare-earth Iron Permanent Magnets* (Oxford: Clarendon Press)
- [44] Stevens K W H 1951 Matrix Elements and Operator Equivalents Connected with the Magnetic Properties of Rare Earth Ions *Proc. Phys. Soc.* **65** 209-215
- [45] Hutchings M T 1964 Point-Charge Calculations of Energy Levels of Magnetic Ions in Crystalline Electric Fields

Solid State Phys. **16** C 227-273

- [46] Smith D and Thornley J H M 1966 The use of "operator equivalents" *Proc. Phys. Soc.* **89** 779
- [47] Kuz'min M D 2005 Shape of Temperature Dependence of Spontaneous Magnetization of Ferromagnets: Quantitative Analysis *Phys. Rev. Lett.* **94** 107204
- [48] Miura D and Sakuma A 2019 Non-collinearity Effects on Magnetocrystalline Anisotropy for R₂Fe₁₄B Magnets *J. Phys. Soc. Jpn.* **88** 044804
- [49] Daisuke M, Sasaki R and Sakuma A 2015 Direct expressions for magnetic anisotropy constants *Appl. Phys. Express* **8** 113003
- [50] Skomski R 1994 The screened-charge model of crystal-field interaction *Philos. Mag. B* **70** 175
- [51] Skomski R, Brennan S and Coey J M D 1995 Crystal-Field Screening in Metallic Multilayers *J. Mag. Soc. Japan* **19** 49